Nano copper-modified GO and CNTs for enhanced the epoxy resin composite thermal properties

Author links open overlay
panelMiao Yuan [a], Yi Zhang [a], Fei Xie [a], Hui Yang [b], Carla Bittencourt [c], Rony Snyders [c], Wenjiang Li [a]

Show more

Add to Mendeley

Share

Cite

https://doi.org/10.1016/j.apsusc.2025.162616Get rights and content

Abstract

Efficient heat dissipation and reduced interface thermal resistance have become an important factor in the advancement of modern electronics. Herein, high aspect ratio Cu nanowires (Cu NWs) and uniform dispersed copper nanoparticles (Cu NPs) were in-situ grown on reduced graphene oxide (rGO) and carbon nanotubes (CNTs) using an one-pot hydrothermal method to obtain a Cu-rGO-CNTs hybrid (CuGNT). The CNTs were carboxylated through acid treatment, which enhanced their hydrophilicity. The creation of the well-dispersed Cu NPs and the high aspect ratio Cu NWs was aided by rGO that was transformed from GO throughout the synthesis. The CuGNT hybrid was used as fillers uniformly dispersed in an epoxy resin (EP) matrix, forming an epoxy composite (CuGNT-EP). The filler formed a 3D-interconnected network, which significantly enhanced the thermal conductivity (the thermal conductivity enhancement factor 87.37 %) of the pure epoxy resin even at low filler levels (relative to 2 wt% of EP content) and maintain high tensile strength (33.76 Mpa). Moreover, the filler has excellent thermal stability and oxidation resistance and the filler does not form a complete conductive path, thereby meeting the requirements for antistatic functionality (> 10^9 Ω·m). Therefore, the CuGNT-EP composite shows great potential for semiconductors, IC packaging, and aerospace applications.

Graphical abstract

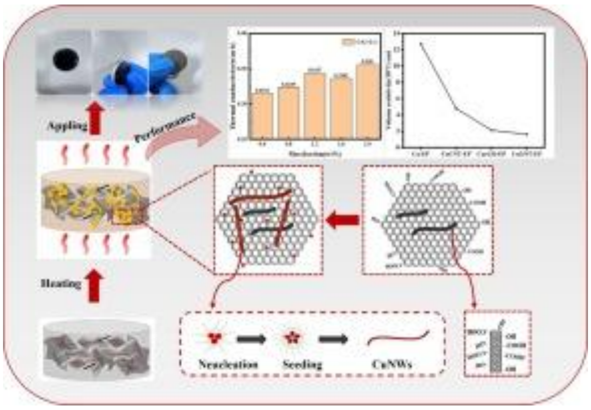

- Previous article in issue
- Next article in issue

Keywords

Thermal properties

Graphene oxide

Low filler levels

Carbon nanotubes

1. Introduction

The requirement for effective thermal management has become increasingly important in various domains, including high-power electronics, heat exchangers, aerospace applications, and integrated circuit packaging, where rapid heat transfer and dissipation are essential [1], [2], [3], [4], [5]. Recent investigations have focused on lightweight materials, particularly polymer matrix composites (PMCs) [6]. Among these, epoxy resin, a widely used thermosetting material, demonstrates good chemical resistance, thermal stability, and ease of processing, along with high strength and post-heat curing [7]. However, traditional EP-based materials are not suited for many sophisticated applications due to their poor electrical and thermal conductivity. Therefore, a variety of techniques, such as adding fillers, have been used to improve electrical and thermal conduction properties of EP [8], [9]. Metallic fillers, such as Ag, Cu, and Au, have been identified as effective means to improve EP properties [10]. Notably, copper is a cost-effective alternative to silver and gold, possessing a high thermal conductivity of 390 W/mK [11]. Recent reports have highlighted the potential of Cu NWs as fillers for EP due to their exceptional thermal conductivity, flexibility, and electrochemical properties [12], [13]. However, the susceptibility of Cu NWs to oxidation hinders practical applications [14], [15], [16]. The creation of core–shell or coating structures is the main strategy used today to reduce the oxidation of Cu NWs [17], [18]. Techniques include encapsulating Cu NWs with polypyrrole [19], forming copper@nickel nanowires or core–shell structure [20], and developing copper nanowires@reduced graphene oxide (Cu NWs/rGO) core–shell structure [21]. Additionally, atomic layer deposition has been used to coat Cu NWs with Al:ZnO films [22].

Graphene, recognized for its excellent thermal properties and air stability, emerges as a promising coating material capable of blocking oxygen and moisture [23]. Shi et al. [24] used chemical vapor deposition (CVD) to prepare graphene films, subsequently transferring them onto Cu NWs. Yang et al. [25] obtained a Cu NW@graphene core–shell structure with superior oxidation stability by combining solution-processed graphene oxide with Cu NWs, followed by mild thermal annealing. Despite these advancements, most current methods for preparing Cu NWs/rGO are characterized by complex multi-step processes that require separate preparation of Cu NWs and rGO. Recent efforts have been made to simplify these procedures through one-pot synthesis methods. For example, Chang et al. [26] obtained rose-like Cu NWs@rGO composites by heating $Cu(NO_3)_2$ in an oil bath, using catechin as a reducing agent, ethylenediamine (EDA) as a capping agent, and GO as the coating layer. The resulting Cu NWs in CuNWs@rGO hybrids exhibited diameters and lengths of approximately 200 ± 4 nm and 4 ± 2 um, respectively. Similarly, Zhang et al. [27] created bridging-oriented copper nanowire-graphene hybrids that are appropriate for air-stable flexible electrodes and solution processing, using ethylene glycol as the agent that reduces. However, the stability of the bridging structures remains a concern, as some Cu NWs are still exposed to air. Furthermore, achieving a substantial enhancement in thermal conductivity required a high filler loading exceeding 20 vol% [12], [28], [29]. For example, Zhang et al. [29] reported an increase in the thermal conductivity of polypropylene (PP) to 1.07 W/mK by incorporating a continuously segregated Al_2O_3 filler at a loading of 27.5 vol%. However, such elevated filler loadings are not ideal, as they increase fabrication costs, complicate processing, and significantly deteriorate mechanical properties.

In this study, we present a novel approach for in-situ synthesis of high aspect ratio Cu NWs and uniform ultra-small Cu NPs on rGO and CNTs through a one-pot hydrothermal method, resulting in the formation of the CuGNT hybrids. The well-dispersed graphene-layer-like GNT (rGO and C-CNTs) nanostructure, uniformly decorated with nano-copper, effectively reduces the agglomeration and oxidation of Cu. This hybrid is subsequently used as a reinforcement material within an EP matrix. The structural and morphological characteristics of the hybrids and epoxy composites are characterized, and their thermal and electrical properties are evaluated and discussed.

2. Experimental section

2.1. Materials

Graphene oxide aqueous dispersion was purchased from Hangzhou Gaoene Technology. CNTs (purity > 95 %) were purchased from Mr. Nanotechnology. Concentrated sulfuric acid (H_2SO_4) and nitric acid (HNO_3) were provided by Tianjin Jiangtian Chemical Technology Co, LTD. Copper(II) chloride dihydrate($CuCl_2·2H_2O$), hexadecylamine (HDA), Glucose were purchased from Aladdin Industrial Corporation. HDA and glucose from Aladdin. Bisphenol A epoxy resin (E-44) was acquired from Macklin Co, Ltd. 1,2-Cyclohenanedicarboxylic anhydride and 2,4,6-Tris (dimethylaminomethyl) phenol were sourced from Aladdin Co, Ltd. No additional distillation was necessary because every other reagent used in this experiment was at least analytical grade.

2.2. Acid treatment of CNTs for surface functionalization with oxo groups

The purchased CNTs underwent an acid treatment process. Initially, 0.5 g of CNTs was accurately weighed and placed in a beaker. Subsequently, 15 mL of HNO_3 and 45 mL of H_2SO_4 were slowly added to the beaker. The resultant mixture was then heated in a magnetic stirring water bath maintained at a constant temperature of 60 °C for 3 h. Upon completion of the reaction, the resulting suspension was diluted and subjected to multiple washes with deionized water. The carboxylated CNTs (C-CNTs) were subsequently freeze-dried at −50 ℃ for 48 h under a pressure of less than 25 Pa. As shown in Fig. S1, these indicate the successful functionalization of the CNTs with oxygenated functional groups.

2.3. Preparation of CuGNT hybrids

CuGNT nanostructures were synthesized using a green and efficient one-step hydrothermal method, followed by recovery and freeze-drying. Initially, precise amounts of $CuCl_2·2H_2O$, glucose, and hexadecylamine were dissolved in 50 mL of deionized water under continuous magnetic stirring. In parallel, C-CNTs and GO were mixed in a 1:1 ratio and dispersed in water via ultrasonication for 30 min to achieve uniform dispersion. The dispersed carbon mixture was then gradually introduced into the $CuCl_2$ solution, maintaining a controlled Cu-to-carbon (C-CNTs + GO) weight ratio of approximately 10:3. The resulting suspension was stirred continuously for 8 h to promote uniform mixing and interaction among the components.

Following complete mixing, the suspension was placed in stainless steel autoclaves lined with Teflon and hydrothermally treated for 20 h at 120 °C. Following the reaction, the autoclaves were allowed to cool naturally to room temperature. The reaction products were then separated by centrifugation using a 1:1 (v/v) mixture of isopropanol and deionized water at 7000 rpm for 6 min, effectively removing unreacted materials and byproducts. The isolated CuGNT hybrids were redispersed in a small amount of deionized water and subjected to freeze-drying at −55 °C for 48 h under vacuum (pressure < 20 Pa). This process yielded a stable, well-dispersed composite filler powder, suitable for further applications.

2.4. Preparation of epoxy composites

Initially, the pure epoxy resin was heated to 60 °C for several minutes to improve its fluidity. Upon achieving the desired viscosity, a predetermined amount of CuGNT hybrid filler was added to the epoxy resin. The mixture was then subjected to magnetic stirring for 40 min to ensure thorough dispersion of the filler within the resin matrix. Following this, an appropriate amount of curing agent was added to the mixture. The resulting mixture was magnetically stirred until a homogeneous blend of filler and resin was attained. Subsequently, the homogenous mixture was put in a vacuum oven at 60 °C for approximately 45 min to eliminate entrapped air bubbles. After the degassing process, the composite was transferred to an oven for a stepwise curing process: first at 90 °C for 2 h, followed by an additional 2 h at 120 °C (Scheme 1).

1. Download: Download high-res image (161KB)
2. Download: Download full-size image

Scheme 1. Schematic route for the preparation of CuGNT-EP coating.

2.5. Characterization methods

X-ray diffraction (XRD) was used to evaluate the samples' crystalline phase using a Smart Lab 9 KW equipment (Rigaku). A Frontier Mid-IR FTIR spectrometer (Perkin Elmer) was used to measure Fourier transform infrared (FTIR) spectra in order to determine which functional groups were present in the samples. The microstructure of the composites were characterized by scanning electron microscopy (SEM) using a Quanta FEG 250 instrument (FEI) and HRTEM with FEG (Talos F200 X, FEI). Additionally, Raman spectroscopy was performed using a Horiba Evolution high-resolution laser confocal micro-Raman spectrometer to assess the compositional and structural integrity of the composites. Surface chemical compositions and the elements in the composites were determined through XPS. The thermal stability of the samples was assessed using a thermogravimetric analyzer (Perkin Elmer). Electrical properties, specifically sheet resistance, were measured using a digital multimeter (VC9806, Victor). The thermal conductivity of the epoxy composites was measured using a DRL-III-P thermal conductivity tester based on the heat flow method. Surface temperature variations of the composites during heating were monitored with an infrared thermal imager (TIS60 +).

3. Results and discussion

3.1. Fillers and composite characterization

Fig. 1 illustrates the XRD patterns of CuGNT, CurGO, CuCNT, and pure Cu NWs. As expected, three distinct peaks are observed at 43.2°, 50.3°, and 74.1°, which correspond to the (111), (200), and (220) crystal planes of face-centered cubic (FCC) Cu [30], [31], respectively. Additionally, the reduced carbon materials (rGO and CNTs) exhibit a low-intensity peak at 21.06°, primarily attributed to the partial restoration of the sp^2 hybridization characteristic of graphite [30], [32].

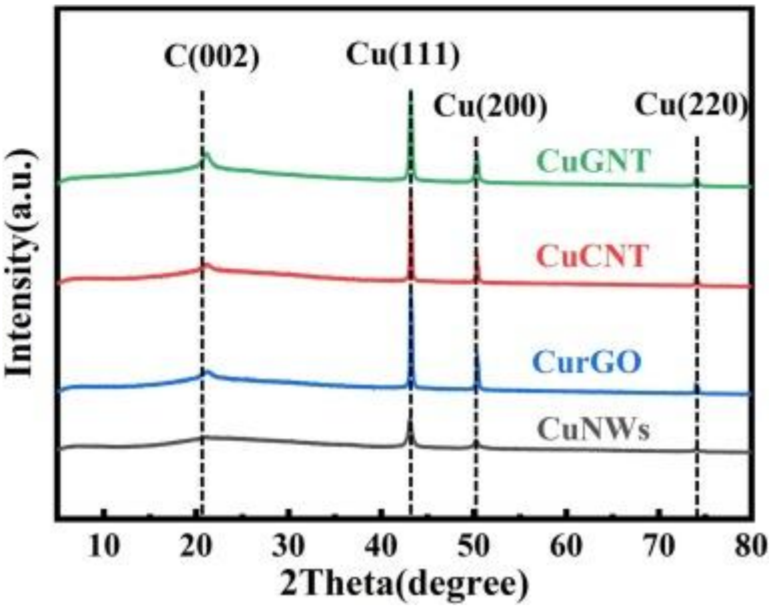

Fig. 1. XRD pattern of Cu NWs, CurGO, CuCNT, and CuGNT.

Fig. 2a compares the FTIR spectra of GO, C-CNT, and CuGNT. The spectrum of GO exhibits several characteristic peaks, including a broad peak at 3408 cm^{-1}, attributed to the stretching vibration of O–H groups from adsorbed water and a peak at

1408 cm^{-1} corresponding to the bending vibration of O–H. In addition, the absorption band at 1737 cm^{-1} is associated with the stretching vibration of C=O from the carboxyl groups. Weak peaks at 1241 cm^{-1} and 1060 cm^{-1} are related to the epoxy (O-C-O) and alkoxy (C-O) functional groups present at the edge of GO, respectively. The sharp peak at 1620 cm^{-1} further confirms the presence of adsorbed water [30], [33]. In contrast, the FTIR spectrum of CuGNT shows a significant reduction in the intensity of the aforementioned peaks, indicating that GO has been largely reduced. Nevertheless, a few hydroxyl groups persist, likely due to the limited efficacy of glucose as a reducing agent [33]. This observation also suggests an interaction between Cu NWs and the remaining hydroxyl groups [33], [34].

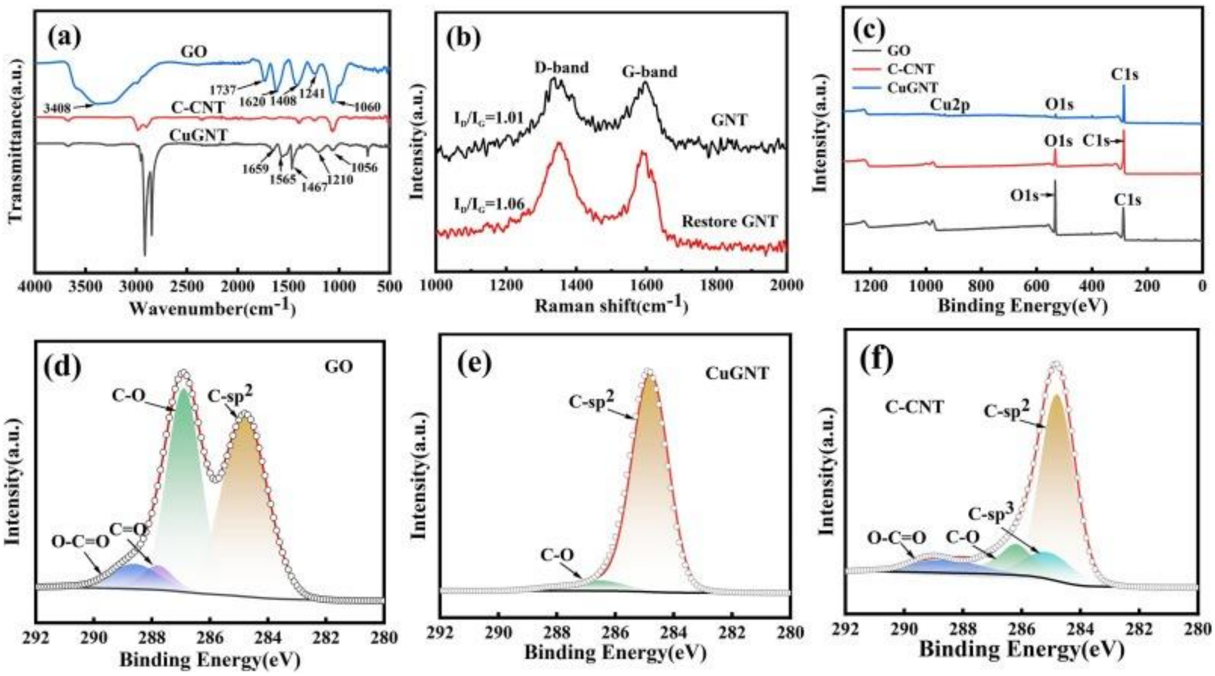

1. Download: Download high-res image (487KB)
2. Download: Download full-size image

Fig. 2. (a) FTIR spectra of GO, C-CNTs, and CuGNT, (b) Raman spectra of GNT and rGNT, (c) Survey XPS spectrum for GO, C-CNTs and CuGNT, The C1s XPS spectra for (d) GO, (e) CuGNT and (f) C-CNTs.

The Raman spectra of GNT and reduced GNT are shown in Fig. 2b. The most prominent band in the GNT spectrum is the D band, observed at approximately 1355 cm-1, which is indicative of defects and disorder within the carbon lattice. A second significant band is the G band, centered at 1588 cm-1, corresponding to the E2g phonon mode of sp^2-bonded carbon atoms. The calculated D/G ratios for GNT and reduced GNT are 1.01 and 1.06, respectively. The observed slight increase in the D/G ratio (ID/IG) suggests that the reduction of GNT was successful [35], [36].

Fig. 2c-f presents the XPS survey spectra and C1s XPS spectra of GO, CuGNT, and C-CNTs. In Fig. 2c, a notable reduction in the oxygen content of CuGNT compared to GO is observed, suggesting a successful reduction of the GNT. The C1s peak was deconvoluted using XPS-PEAK software into three components centered at 284.8 eV (sp^2 C), at 286.9 eV (–C–O–), and at 288.6 eV (–CO–O–). Fig. 2d-f further demonstrate a decrease in the relative content of –C–O– and –CO–O– functionalities, alongside the complete absence of the –CO– peak in CuGNT, indicating a diminished presence of –COOH and–OH functional groups. These observations align with the FTIR analysis, confirming the successful reduction of CuGNT [33], [37].

Building upon these findings, the proposed formation mechanism for CuGNT is illustrated in Fig. 3. Multilayer GNT sheets are separated during ultrasonic processing. Subsequently, Cu^{2+} ions are drawn to oxygen functionalities of GNT due to coordination interactions with –OH groups. Upon the introduction of HDA, various Cu^{2+}-HDA-GNT-Cu^{2+} clathrates may form, driven by the active hydroxyl groups of GNT, which not only stabilize Cu^{2+} ions but also adsorbed HDA molecules [30], [33]. On the one hand, the active hydroxyl groups of GNT can function as reducing sites for Cu^{2+} ions. As temperature increases, some adsorbed Cu^{2+} ions are reduced to Cu, which subsequently grow into ultra-small Cu NPs [38]. Conversely, other Cu^{2+} ions are induced to grow into Cu NWs in the presence of HDA-GNT, with glucose serving as a mild and environmentally friendly reducing agent for the reduction of GNT to rGNT [39]. It is proposed that the HDA-GNT complex exhibits a superior capping effect relative to HDA alone, attributable to the synergistic enhancement provided by GNT. The HDA-GNT complex selectively passivates the [100] facet of copper, facilitating the deposition of Cu^0 on the [111] crystal plane and the consequent formation of ultra-long Cu NWs along the [110] direction. Thus, excellent quality Cu NWs and uniformly ultrasmall Cu NPs are insitu synthesized on the rGNT, forming the CuGNT hybrids (Fig. 3) [30].

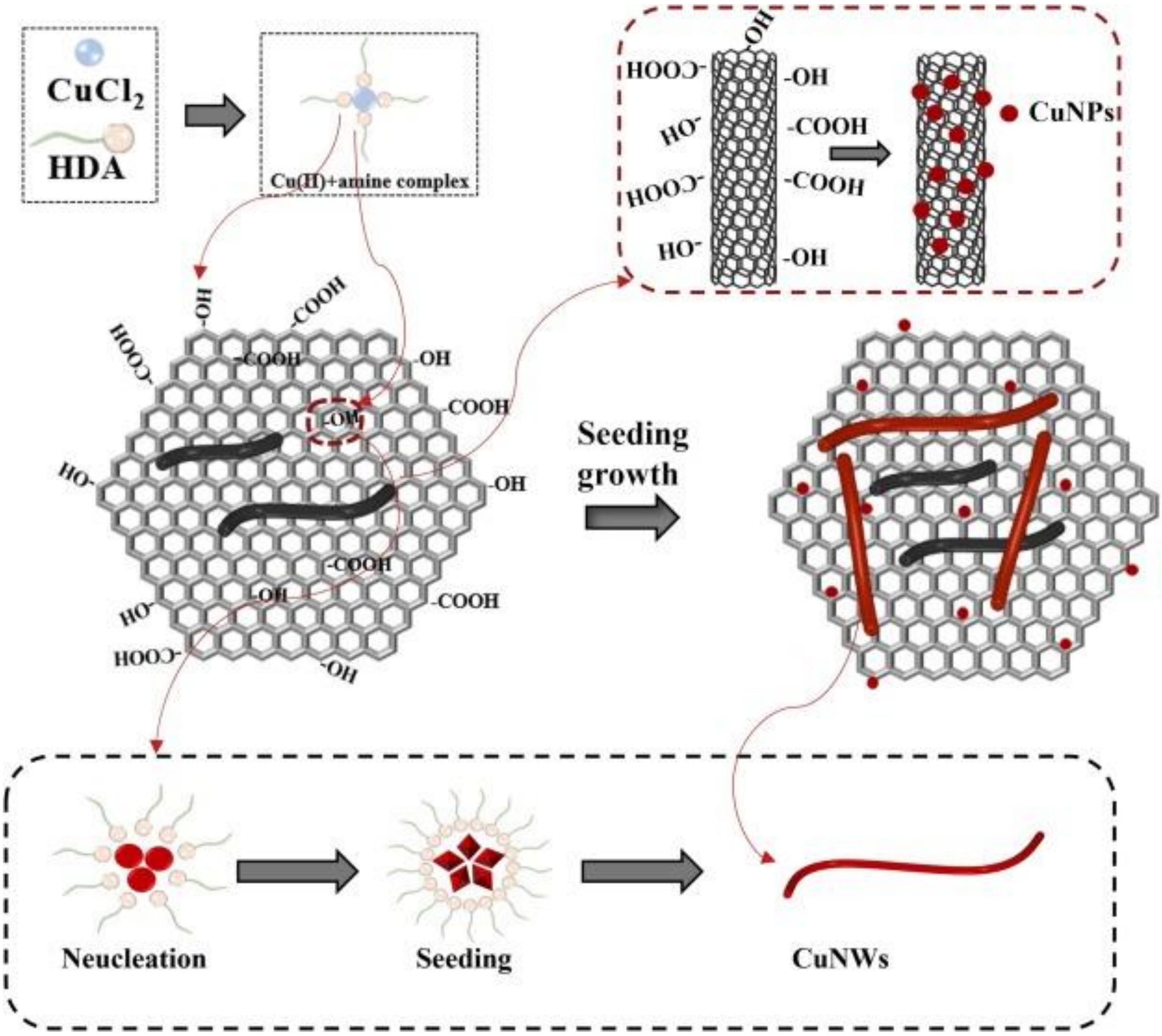

Fig. 3. Schema of the Cu NWs synthesis mechanism.

The SEM images illustrating the morphology of Cu NWs and CuGNT hybrids are shown in Fig. 4. The Fig. 4a shows Cu NWs with an average diameter of 40 ± 5 nm and Fig. 4d is the corresponding magnified image. Notably, the incorporation of GNT during the synthesis process led to Cu NWs with lengths in the range of 60–80 μm (Fig. S2), significantly larger than that of pure Cu NWs. This observation suggests that GNT plays an essential role in controlling the growth of Cu NWs, likely due to its enhancing effect on the molecular capping properties of HDA [30]. Fig. 4b presents the image of GNT and in Fig. 4e, the corresponding magnified image. In the well-mixed carbon solution, carbon nanotubes are seen attached to the surface of the graphene layer. This attachment is likely due to π-π interactions, along with hydrogen and chemical bonds between the CNT walls and the graphene layers [10]. Furthermore, as illustrated in Fig. 4c and 4f, the high aspect ratio Cu NWs are observed to grow in situ between the rGO. This structural arrangement is anticipated to substantially impede the permeation of oxygen and water molecules, thereby enhancing the oxidation resistance of Cu NWs [30], [33]. Additionally, due to the increased length of the nanowires, a reduced quantity of nanowires is needed to form networks, which further improve the thermal conductivity [40], [41].

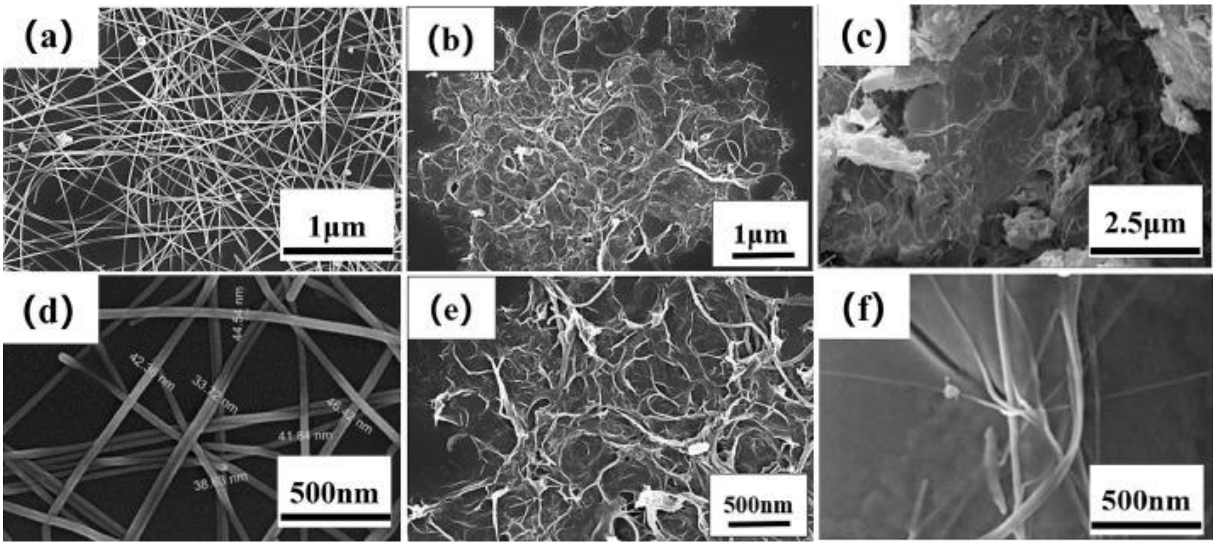

Fig. 4. (a, d) SEM image of Cu NWs, (b,e) SEM image of GNT nanocomposite, (c,f) SEM image of CuGNT nanocomposite.

The HRTEM images of Cu NWs and CNTs within CuGNT hybrids are presented in Fig. 5. Fig. 5a and 5b clearly depict the presence of Cu NWs and CNTs either on the the interlayers of rGO. Fig. 5c-f show the elemental dot-mapping images of the CuGNT hybrid. The elemental map in Fig. 5d and 5e reveals a high-density signal distribution of carbon, indicating the presence of CNTs. Similarly, the presence of CuNWs is confirmed by the maps in Fig. 5d and 5f, which display a copper signal distribution. Additionally, the widespread distribution of copper dots throughout the surfaces of rGO suggests that ultra-small copper nanoparticles (Cu NPs) were formed and uniformly decorated on the rGO surface, coinciding with the growth of CuNWs [30].

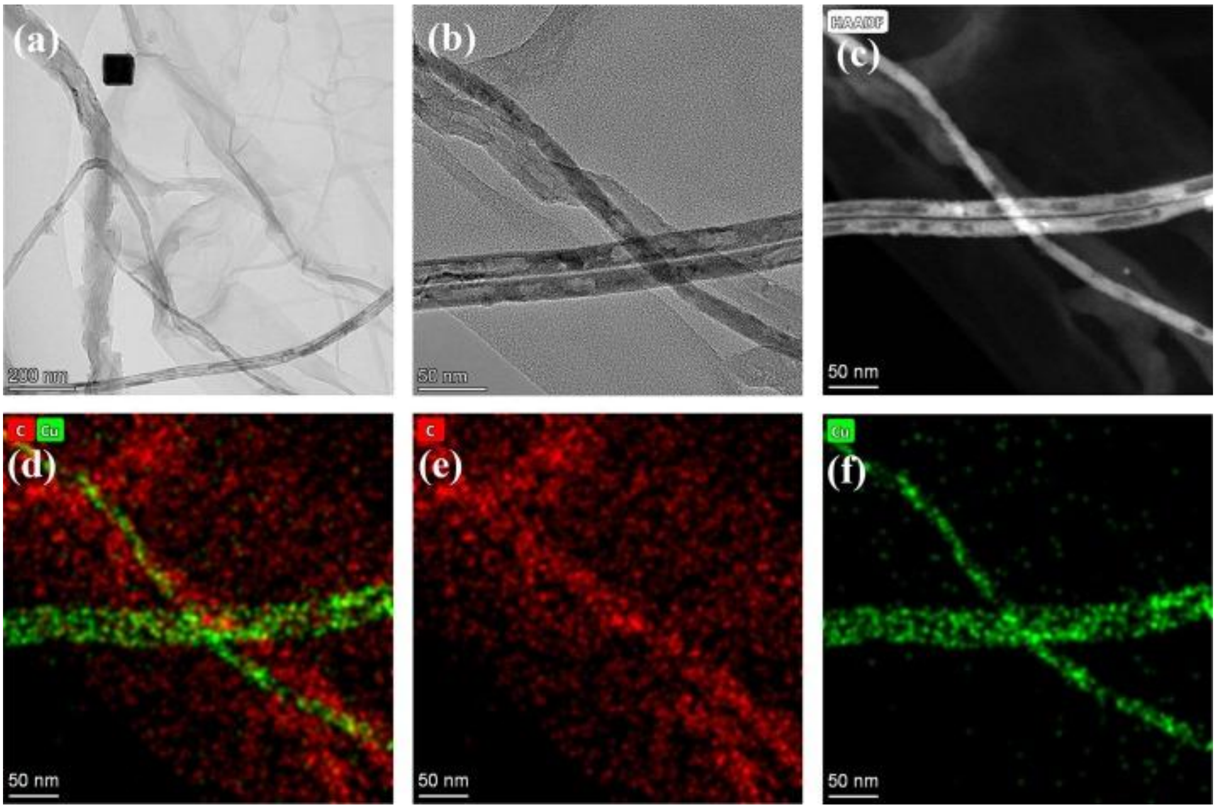

Fig. 5. (a,b) HRTEM image of CuGNT hybrid (c) HADDF image of CuGNT hybrid, (d,e) carbon elemental mapping (red), and (d,f) Cu elemental mapping (green) of CuGNT hybrid. (For interpretation of the references to color in this figure legend, the reader is referred to the web version of this article.)

3.2. Oxidation resistance and thermal stability of CuGNT fillers with coated nanostructures

Fig. 6 shows TGA cures of CuNWs, CuCNT, CurGO and CuGNT. CuCNT, CurGO and CuGNT showed a significant mass loss during 319.5–482.3℃, which was due to the initial decomposition of unstable oxygen-containing functional groups of the material, further indicating that the reduction degree was incomplete. The mass loss of CuCNT, CurGO, CuGNT and CuNWs are 27.95 %, 28.96 %, 27.47 %, and 53.81 %, respectively. From 482.3 to 800℃, the mass loss of sample CuNWs, CuCNT, CurGO and CuGNT are 11.93 %, 19.01 %, 22.41 %, 28.71 %, the decomposition rate and mass loss of CuGNT are significantly reduced, and the mass loss of CuNWs is the largest, which indicates that the existence of GNT structure can significantly improve the thermal stability of the composites.

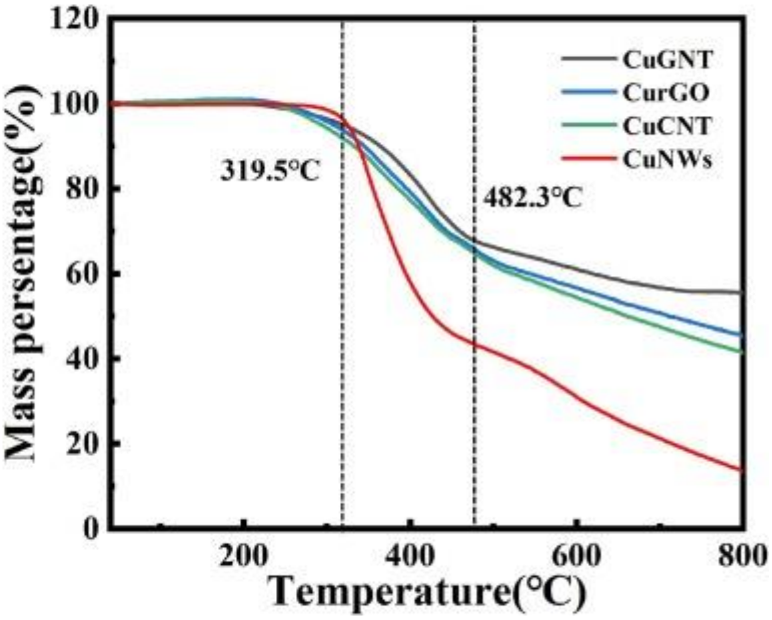

Fig. 6. TGA pattern of Cu NWs, CurGO, CuCNT, and CuGNT.

Fig. 7a shows images of Cu NWs and CuGNT dispersed in isopropanol after storage for varying duration times. Visually, the composite maintains its reddish-black color even after one month, exhibiting no discernible changes in appearance. This observation allows for a preliminary conclusion that the CuGNT nanostructure demonstrates remarkable temporal stability [33]. To further investigate the temporal stability of the CuGNT, XRD analysis was used. The XRD patterns of CuGNT, exposed to ambient air at room temperature over several days, are illustrated in Fig. 7b. The characteristic peaks of the Cu NWs located at 43.4°, 50.4°, and 74.2°, corresponding to the (111), (200), and (220) crystal planes of metallic Cu, remain unchanged over time. Notably, there are no observable shifts in peak positions, nor do new oxidation phases emerge after 40 days of exposure to air [33].

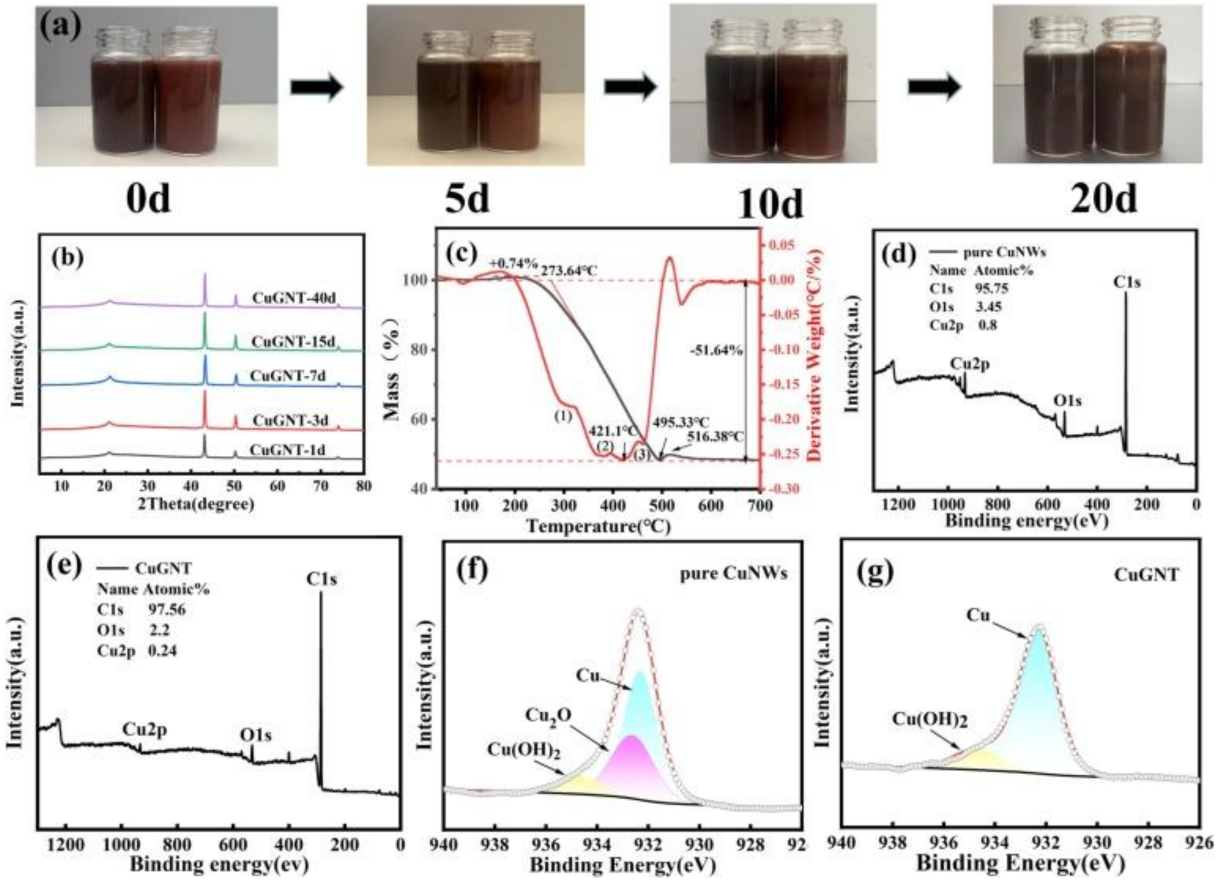

1. Download: Download high-res image (606KB)
2. Download: Download full-size image

Fig. 7. (a) Freshly-prepared Cu NWs (right) and the CuGNT (left) dispersed in isopropanol after storage in air for 0, 5, 10, and 20 days, (b) XRD patterns of the Cu NWs and the CuGNT placed in air for 1, 3, 7, 15 and 40 days, (c) DTC-TG curve of the CuGNT with coating nanostructure, survey XPS spectra for (d) Cu NWs and (e) CuGNT, The C1s XPS spectra for (f) Cu NWs and (g) CuGNT hybrid.

Nano-sized copper is susceptible to oxidation upon exposure to air; however, the addition of rGO during the synthesis effectively moderates this vulnerability. The antioxidative effect of the rGO coating is confirmed by thermo-differential analysis [33]. As shown in Fig. 7c, the TG curve indicates an initial mass increase of approximately 0.74 % attributable to the oxidation of a minor fraction of exposed Cu NWs and Cu NPs. Subsequently, the rGO coating begins to oxidize at approximately 273.6℃, following the reaction pathway C (s) → CO_2 (g). At 495.3℃, the weight loss reaches 51.7 %. The DTG curve shows three distinct weight loss events, likely due to the oxidation of exposed Cu NWs and Cu NPs that lack protective coating. The first weight loss event (1) may correspond to the oxidation of a small quantity of uncoated copper. The subsequent events (2) and (3) may be associated with the exposed CNT participating in the reaction, resulting in mass variations. Following the C (s) → CO_2 (g) pathway, the Cu NPs attached to the inner wall are oxidized. Additionally, fully exposed Cu NWs and Cu NPs undergo further oxidation beyond 495.3℃, with a slight mass decrease at 516.4℃, likely due to the continued formation of CO_2 from residual carbon particles. The rGO and CNT coatings significantly enhance the oxidation resistance of nano-sized copper, even at elevated temperatures, with oxidation occurring primarily when the protective coating is damaged.

Fig. 7d-g display the Cu 2p3/2 peak fitting findings and XPS survey spectra for Cu NWs and CuGNT hybrids. The Cu NWs sample's XPS quantitative analysis shows 95.8 % carbon and 3.5 % oxygen, which are probably caused by leftover organic materials on the surface [30], [42]. In contrast, the CuGNT hybrids exhibit an increase in the relative carbon content to 97.7 % and a decrease in relative oxygen content to 2.2 %, attributed to the incorporation of GNT. Fig. 7f illustrates how the Cu 2p spectrum for Cu NWs may be broken down into three distinct components, which correspond to Cu, Cu_2O and $Cu(OH)_2$ at 932.6, 932.9 and 934.7 eV, respectively [43]. Interestingly, the Cu 2p3/2 peak of CuGNT hybrids (Fig. 7g) shows no components belonging to CuO or Cu_2O, suggesting that metallic Cu remained almost unoxidized during synthesis. This observation suggests that the graphene coating effectively inhibited the ingress of moisture and oxygen, thereby enhancing the oxidation resistance of the CuGNT nanocomposites, in agreement with previous findings [30], [33]. Therefore, the above experimental results confirm the superior protective capability of the graphene sheets covering the Cu NWs, effectively preventing oxidation. Collectively, these experimental results confirm the superior protective efficacy of the graphene sheets enveloping the Cu NWs, effectively preventing oxidation.

3.3. Thermal conductivity of the epoxy-based composites

The optimization of thermal conductivity can be achieved through the combination of multiple fillers possessing high thermal conductivity. Variations in the amount of these fillers within a composite can yield different thermal conductivity values; thus, it is necessary to establish the optimal ratio to maximize thermal conductivity while maintaining a consistent total filler load. In the present study, the detailed calculation method of thermal conductivity is shown in Fig. S3. The optimal thermal conductivity was attained with a Cu to C (graphene oxide) ratio of approximately 10:3 (Fig. S4). Fig. 8a shows the variation in thermal conductivity of the CuGNT-EP composite as a function of the ratio of rGO to CNTs within a hybrid filler while keeping the total load constant at 2 wt%, along with a fixed Cu content and a constant total C content (the combined content of graphene and carbon nanotubes). The data indicate that thermal conductivity reaches its maximum when the CNT to rGO ratio is 1:1. The thermal conductivity of CuGNT-EP composites with varying filler loadings is displayed in Fig. 8b. The results show that within a specific filler type, an increase in filler content enhances thermal conductivity. The thermal conductivity values of five EP-based samples are shown in Fig. 8c. The thermal conductivity of the pure EP sample is 0.19W $m^{-1}K^{-1}$, which is comparable to the values that have been published [15], [26]. Upon the incorporation of pure nano-copper particles, the thermal conductivity of EP composite rises to 0.3211 W $m^{-1}K^{-1}$, attributable to Cu comparatively superior theoretical thermal conductivity relative to EP. The Cu-rGO-EP composite further enhances thermal conductivity to 0.3416 W $m^{-1}K^{-1}$, whereas the CuCNT-EP composite achieves a thermal conductivity of 0.3448 W $m^{-1}K^{-1}$. Among the five samples, the CuGNT-EP composite notably has the highest thermal conductivity, reaching 0.356 W $m^{-1}K^{-1}$, which represents the 87.4 % increase compared to pure EP. This remarkable improvement in thermal conductivity, despite maintaining the same weight fraction of fillers as observed in the Cu-EP, Cu-rGO-EP, and CuCNT-EP composites, suggest the formation of a well-dispersed three-dimensional (3D) network of CuGNT nanostructures within the EP matrix (Fig. 8d). This 3D network likely facilitates continuous pathways for phonon transport, thereby optimizing heat transfer, as supported by the SEM results shown in Fig. 4.

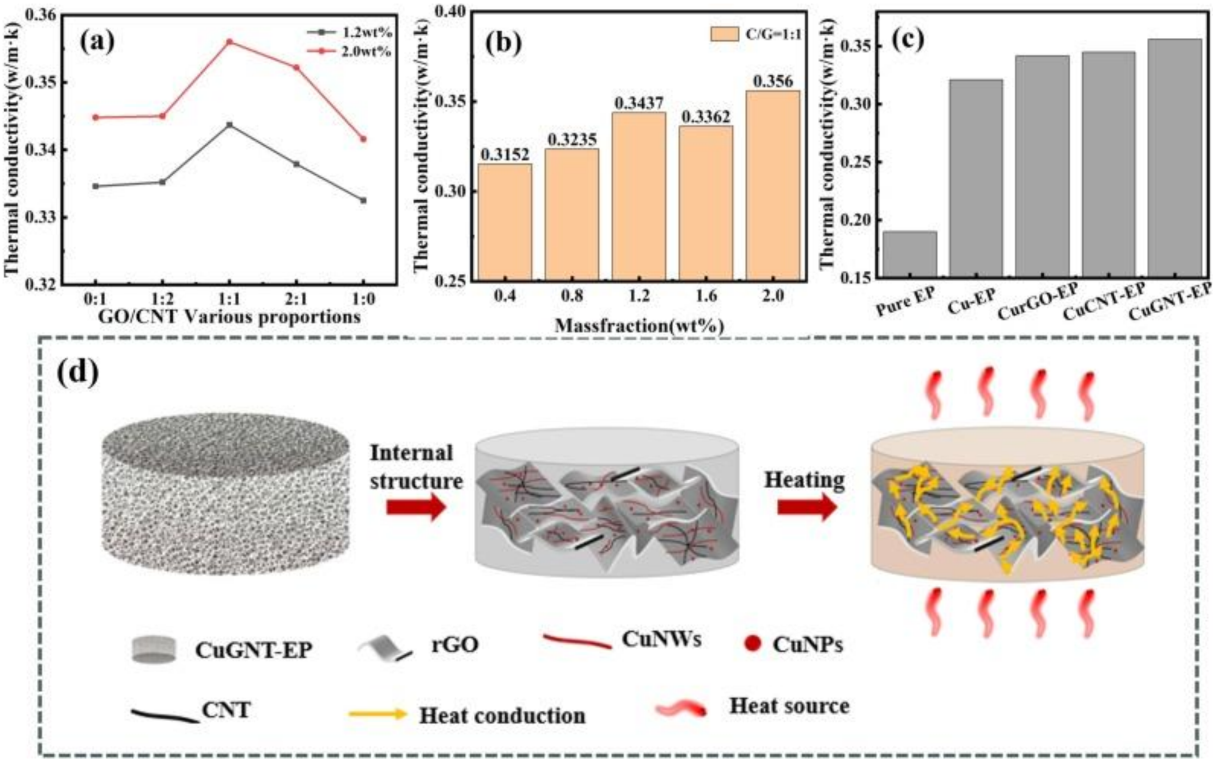

Fig. 8. (a) The thermal conductivity of CuGNT-EP composites with different GO/CNT, (b) The thermal conductivity of CuGNT-EP composites with different filler loadings, (c)The thermal conductivity of pure EP, Cu-EP, CurGO-EP, CuCNT-EP, and CuGNT-EP samples, (d) Schematic illustration of the heat transfer in the CuGNT-EP composites.

Table 1 presents the comparison of thermal performances between the CuGNT-EP composites and some reported results. The filler formed a 3D-interconnected network, which significantly enhanced the thermal conductivity (87.37 %) of the pure epoxy resin even at low filler levels (2 wt%) in this work. This likely provided continuous pathways for phonon transport, resulting in efficient heat transfer.

Table 1. Performance comparison of thermal conduction between this work's findings and previous results.

Sample	Thermal conductivity (W $m^{-1}K^{-1}$)	Fraction (wt%)	Reference
CuGNT-EP	0.356	2.0	This work
AgNPs-PEEK	0.27	2.0	[44]
Al/GO-EP	0.25	3.0	[45]
GO-EP	0.36	3.0	[45]
Ag/rGO-NFC	0.26	9.6	[46]
BNNs-ANF	0.31	10.0	[47]
CNT/CNF-PCMs	0.32	10.0	[48]
Graphene-PCMs	0.25	10.0	[49]

By combining Cu-rGO-CNT, the exceptional thermal conductivity of copper is synergistically enhanced with the 3D network structure, which significantly increases the thermal conductivity in CuCNT-EP composites. Tocomposites.To elucidate the mechanism underlying this enhancement in thermal conductivity, a heat conduction model is proposed, as depicted in Fig. 8d. The 3D CuGNT nanostructures formed within the EP matrix facilitate connections among CuNWs and create pathways that promote both electrical and thermal conduction. The establishment of a continuous heat conduction network markedly increases the thermal conductivity of the composites, as more heat is effectively directed along these thermally conductive pathways[10], [50], [51].

3.4. Thermal properties of the composites

As the samples absorbed heat and subsequently dissipated it to their surroundings, variations in surface temperature were meticulously recorded to illustrate the heat transfer capabilities of each composite. To elucidate the mechanisms underlying the enhancement of thermal conductivity, infrared thermal imaging was used to monitor the surface temperature fluctuations of the composites: EP, Cu-EP, CurGO-EP, CuCNT-EP, and CuGNT-EP during the heating process. A heating platform was preheated to 100 °C and maintained at this temperature for one hour to ensure experimental consistency.

The composites were then concurrently put on the heating platform, initially at room temperature. The room-temperature composites were then put on the heating platform at the same time. As the samples absorbed heat and transferred it to their surroundings, surface temperature variations were recorded, providing a clear representation of the heat transfer capabilities of each composite. Fig. 9a-b displays the thermal images alongside the corresponding surface temperature variation curves for the different composites. Notably, the CuGNT-EP composite exhibited the highest rate of temperature increase among all the tested composites.

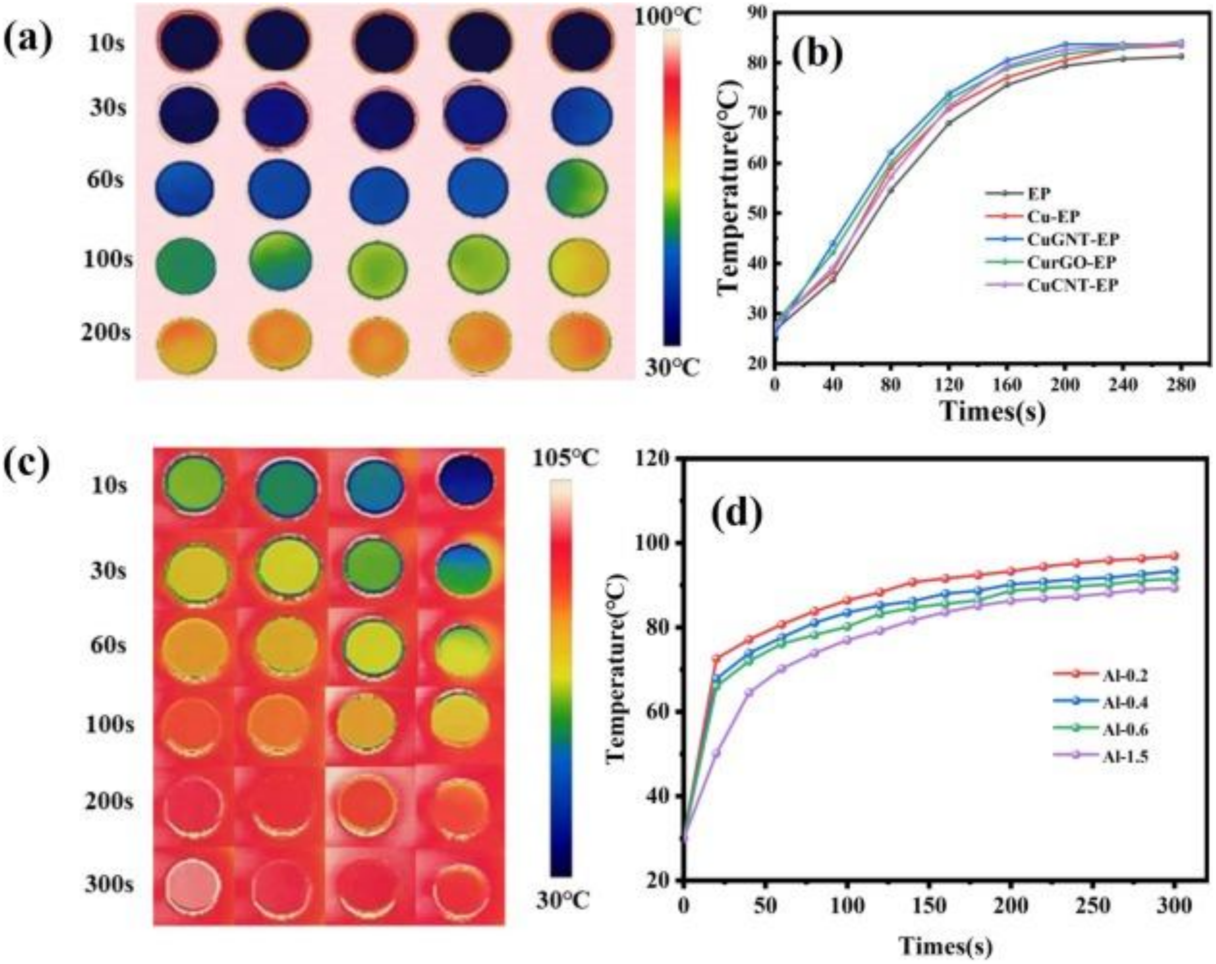

Fig. 9. The 4 mm of pure EP, Cu-EP, CurGO-EP, CuCNT-EP, CuGNT-EP for (a) infrared thermal images and (b) corresponding hot spot temperature variations with time, (c) infrared thermal images and (d) corresponding hot spot temperature variations with time of Coatings of different thicknesses are applied to the aluminum sheet.

To investigate the influence of coating thickness on heat transfer, aluminum sheets with a thickness of 3 mm (after degreasing treatment) were coated with filler layers of varying thicknesses (Fig. S5): 0.2 mm, 0.4 mm, 0.6 mm, and 1.5 mm, respectively, as shown in Fig. 9c-d. The results indicate that thinner coatings enhance the thermal conductivity of the composite, likely attributable to the decreased thickness of the coating layer, which shortens the heat transfer pathway.

Furthermore, to demonstrate the heat transfer properties of the composites, a water evaporation test was conducted. Five composite samples were placed on a heating platform preheated to 120 °C, after which 20 μL droplets of water were applied to their surfaces, and the evaporation process was recorded for each sample. It is noteworthy that variations in surface free energy among the composites resulted in differences in the contact angle and contact area of the water droplets, leading to varying droplet sizes. The water droplets on the CuGNT-EP composite evaporated more rapidly than those on the neat EP, Cu-EP, CurGO-EP, and CuCNT-EP composites, completely disappearing after 878 s (Fig. S6). This observation highlights the superior heat transfer capacity of the CuGNT-EP composite [51].

3.5. Electrical and mechanical properties of the CuGNT-EP composites

The electrical conductivity of the composites was assessed using an electrochemical workstation, with the results of volume resistivity shown in Fig. 10. The incorporation of fillers reduced the electrical resistivity in all four composites. Notably, the epoxy composite containing the CuGNT hybrid filler exhibited the lowest volume resistivity, about 1.8 × 10^{13} Ω·cm. This reduction in resistivity may be attributed to the reaggregation and redistribution of the CuGNT structure, which alters the conductive network within the filler. Despite achieving a minimum volume resistivity, the filler does not form a complete conductive path, thus fulfilling the criteria for antistatic properties (> 10^9 Ω·m) [51], [52].

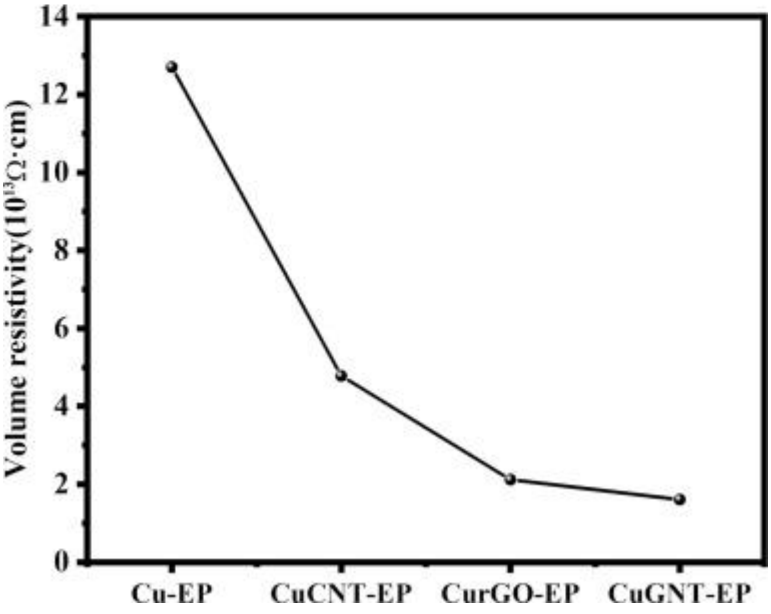

Fig. 10. The electrical resistivity of Cu-EP, CuCNT-EP, CurGO-EP, and CuGNT-EP samples.

In order to further prove the insulation properties of the composite material, an aluminum sheet coated with the composite was integrated into an electrical circuit. The continuity of the circuit was assessed based on the illumination of a small lamp. Longitudinal illumination indicated continuity, while the absence of transverse illumination confirmed effective insulation (Video S1). Consequently, these favorable electrical properties not only extend the potential applications of CuGNT-EP composites in conductive environments, but also avoid the risk associated with static charge accumulation.

In order to explore the mechanical strength of samples with different filler content, the E8 tensile splines of samples (filler content: 0, 1 wt%, 2 wt%, 5 wt% and 10 wt%) were prepared respectively (Fig. S7a). It can be seen from the stress–strain curve of the sample (Fig. S7b) that the fracture is a brittle fracture, and the stress and strain of samples are both the largest, and decrease with the increase of filler content. The maximum stress is 33.76 Mpa and 17.03 Mpa when the filler content is 2 wt% and 10 wt%, respectively. Therefore, the tensile strength of low filler content (2 wt%) is obviously better than that of high filler content (10 wt%). Therefore, the high content of the filler will result in inconvenience to the application of the material.

4. Conclusions

In summary, hybrids of CuGNT were successfully synthesized using a simple and eco-friendly one-pot hydrothermal method. This approach facilitated the in-situ growth of high-quality Cu NWs with a high aspect ratio and uniformly distributed ultra-small Cu NPs on rGO and CNTs. Comprehensive characterization and experimental results confirmed that the composite filler exhibits excellent oxidation resistance and thermal stability. The Cu NWs and Cu NPs served as thermal bridges, effectively connecting adjacent GO sheets and CNTs, thereby establishing a continuous heat transfer pathway with interfacial contact and maintaining good mechanical properties at a mass fraction of 2 wt%. The compatibility between filler and epoxy resin matrix was enhanced, resulting in a composite with a thermal conductivity of $0.356Wm^{-1}K^{-1}$. It was found that thinner filler layers exhibited superior heat dissipation performance, indicating its promising potential in thermal management applications. Additionally, assessments of volume resistivity and continuity tests using a small lamp confirmed that the filler within the composite did not establish a conductive pathway, thereby satisfying the criteria for antistatic functionality. Consequently, the incorporation of CuGNT nanostructures as fillers position epoxy composites for extensive applications in the semiconductor, integrated circuit packaging, aerospace, and automotive industries, presenting substantial opportunities for future advancements.

CRediT authorship contribution statement

Miao Yuan: Writing – original draft, Methodology, Formal analysis, Data curation, Conceptualization. **Yi Zhang:** Supervision, Methodology, Formal analysis. **Fei Xie:** Writing – review & editing, Methodology, Formal analysis. **Hui Yang:** Writing – review & editing. **Carla Bittencourt:** Writing – review & editing. **Rony Snyders:** Writing – review & editing. **Wenjiang Li:** Writing – review & editing, Supervision, Methodology, Funding acquisition, Formal analysis, Conceptualization.

Declaration of competing interest

The authors declare that they have no known competing financial interests or personal relationships that could have appeared to influence the work reported in this paper.

Acknowledgments

This work was financially supported by the Guangxi Key Research and Development Program (2021AB23009) and the National Natural Science Foundation of China (Nos.22271219, 21911530255).

Appendix A. Supplementary data

The following are the Supplementary data to this article:

Supplementary video 1.

Supplementary Data 2.

Data availability

Data will be made available on request.

References

1. [1]

C. Lu, F. Lin, H. Shao, S. Bi, N. Chen, G. Shao, J. Jiang

Carboxylated carbon nanotube/polyimide films with low thermal expansion coefficient and excellent mechanical properties

Polymers, 14 (2022), p. 4565

CrossrefView in ScopusGoogle Scholar

2. [2]

F. Jiang, S. Cui, C. Rungnim, N. Song, L. Shi, P. Ding

Control of a dual-cross-linked boron nitride framework and the optimized design of the thermal conductive network for its thermoresponsive polymeric composites

Chem. Mater., 31 (2019), pp. 7686-7695

CrossrefView in ScopusGoogle Scholar

3. [3]

Y. Yin, B. Jiang, X. Zhu, L. Meng, Y. Huang

Investigation of thermostability of modified graphene oxide/methylsilicone resin nanocomposites

Engineered Science, 5 (2018), pp. 73-78

View in ScopusGoogle Scholar

4. [4]

X. Hu, H. Wu, X. Lu, S. Liu, J. Qu

Improving thermal conductivity of ethylene propylene diene monomer/paraffin/expanded graphite shape-stabilized phase change materials with great thermal management potential via green steam explosion

Adv. Compos. Hybrid Mater., 4 (2021), pp. 478-491

CrossrefView in ScopusGoogle Scholar

5. [5]

L. He

Improve thermal conductivity of polymer composites via conductive network

ES Mater. Manuf., 13 (2021), pp. 1-2

CrossrefGoogle Scholar

6. [6]

M. Vikulova, T. Nikityuk, D. Artyukhov, A. Tsyganov, A. Bainyashev, I. Burmistrov, N. Gorshkov

High-k three-phase epoxy/K1.6(Ni0.8Ti7.2)O16/CNT composites with synergetic effect

Polymers, 14 (2022), p. 448

CrossrefView in ScopusGoogle Scholar

7. [7]

H. Amirbeygi, H. Khosravi, E. Tohidlou

Reinforcing effects of aminosilane-functionalized graphene on the tribological and mechanical behaviors of epoxy nanocomposites

J. Appl. Polym. Sci., 136 (2019), p. 47560

Google Scholar

8. [8]

S. Wu, J. Zhang, R.B. Ladani, K. Ghorbani, A.P. Mouritz, A.J. Kinloch, C.H. Wang

A novel route for tethering graphene with iron oxide and its magnetic field alignment in polymer nanocomposites

Poly, 97 (2016), pp. 273-284

View PDFView articleView in ScopusGoogle Scholar

9. [9]

P. Allia, G. Barrera, T. Nardi, Y. Leterrier, P. Tiberto

Anisotropic magnetic polymer nanocomposite with self-assembled chains of titania-coated magnetite nanoparticles

Mater. Today Commun., 7 (2016), pp. 32-41

View PDFView articleView in ScopusGoogle Scholar

10. [10]

C. Hu, T. Liu, N. Neate, M. Fay, X. Hou, D. Grant, F. Xu

Enhanced thermal and electrical properties by Ag nanoparticles decorated GO-CNT nanostructures in PEEK composites

Compos. Sci. Technol., 218 (2022), Article 109201

View PDFView articleView in ScopusGoogle Scholar

11. [11]

M.H. Al-Saleh, G.A. Gelves, U. Sundararaj

Copper nanowire/polystyrene nanocomposites: lower percolation threshold and higher EMI shielding

Compos. A, 42 (2011), pp. 92-97

View PDFView articleView in ScopusGoogle Scholar

12. [12]

C.-Y. Tsai, T. Zhang, M. Zhao, C.-S. Chang, H.-J. Sue

Preparation of thermally conductive but electrically insulated polypropylene containing copper nanowire

Poly, 236 (2021), Article 124317

View PDFView articleView in ScopusGoogle Scholar

13. [13]

V. Nam, D. Lee

Copper nanowires and their applications for flexible

Transparent Conducting Films: A Review, Nanomaterials, 6 (2016), p. 47

CrossrefView in ScopusGoogle Scholar

14. [14]

S. Polat
Genlik, D. Tigan, Y. Kocak, K.E. Ercan, M.O. Cicek, S. Tunca, S. Koylan, S. Coskun, E. Ozensoy, H.E. Unalan

All-solution-processed, oxidation-resistant copper nanowire networks for optoelectronic applications with year-long stability

ACS Appl Mater. Interfaces, 12 (2020), pp. 45136-45144

CrossrefView in ScopusGoogle Scholar

15. [15]

W. Su, Z. Wang, Z. Chang, F. Geng, S. Yuan, J. Jiang, K. Wang, X. Peng

Mechanically robust and lightweight double-layer bacterial cellulose-CuNWs with photothermal conversion and piezoresistive sensing

Appl. Surf. Sci., 655 (2024), Article 159554

View PDFView articleView in ScopusGoogle Scholar

16. [16]

R. Mehta, S. Chugh, Z. Chen

Enhanced electrical and thermal conduction in graphene-encapsulated copper nanowires

Nano Lett., 15 (2015), pp. 2024-2030

CrossrefView in ScopusGoogle Scholar

17. [17]

J. Song, J. Li, J. Xu, H. Zeng

Superstable transparent conductive Cu@Cu4Ni nanowire elastomer composites against oxidation, bending, stretching, and twisting for flexible and stretchable optoelectronics

Nano Lett., 14 (2014), pp. 6298-6305

CrossrefView in ScopusGoogle Scholar

18. [18]

Y. Li, H. Zhang, B. Wu, Z. Guo

Improving the oxidation resistance and stability of Ag nanoparticles by coating with multilayered reduced graphene oxide

Appl. Surf. Sci., 425 (2017), pp. 194-200

View PDFView articleView in ScopusGoogle Scholar

19. [19]

K. Liu, Y. Li, H. Zhang, Y. Liu

Synthesis of the polypyrrole encapsulated copper nanowires with excellent oxidation resistance and temporal stability

Appl. Surf. Sci., 439 (2018), pp. 226-231

View PDFView articleView in ScopusGoogle Scholar

20. [20]

H. Guo, J. Jin, Y. Chen, X. Liu, D. Zeng, L. Wang, D.-L. Peng

Controllable synthesis of Cu–Ni core–shell nanoparticles and nanowires with tunable magnetic properties

Chem. Commun., 52 (2016), pp. 6918-6921

View in ScopusGoogle Scholar

21. [21]

S. Huang, Q. Zhang, P. Li, F. Ren, A. Yurtsever, D. Ma

High-performance suspended particle devices based on copper-reduced graphene oxide core–shell nanowire electrodes

Adv. Energy Mater., 8 (2018), p. 658

Google Scholar

22. [22]

M. Wang, K.-L. Choy

All-nonvacuum-processed CIGS solar cells using scalable Ag NWs/AZO-based transparent electrodes

ACS Appl. Mater. Interfaces, 8 (2016), pp. 16640-16648

CrossrefView in ScopusGoogle Scholar

23. [23]

J. Liu, G.H. Kim, Y. Xue, J.Y. Kim, J.B. Baek, M. Durstock, L. Dai

Graphene oxide nanoribbon as hole extraction layer to enhance efficiency and stability of polymer solar cells

Adv. Mater., 26 (2013), pp. 786-790

View in ScopusGoogle Scholar

24. [24]

L. Shi, R. Wang, H. Zhai, Y. Liu, L. Gao, J. Sun

A long-term oxidation barrier for copper nanowires: graphene says yes

Phys. Chem. Chem. Phys., 17 (2015), pp. 4231-4236

View in ScopusGoogle Scholar

25. [25]

L. Dou, F. Cui, Y. Yu, G. Khanarian, S.W. Eaton, Q. Yang, J. Resasco, C. Schildknecht, K. Schierle-Arndt, P. Yang

Solution-processed copper/reduced-graphene-oxide core/shell nanowire transparent conductors

ACS Nano, 10 (2016), pp. 2600-2606

CrossrefView in ScopusGoogle Scholar

26. [26]

A.P. Periasamy, J. Liu, H.-M. Lin, H.-T. Chang

Synthesis of copper nanowire decorated reduced graphene oxide for electro-oxidation of methanol

J. Mater. Chem. A, 1 (2013), p. 5973

CrossrefView in ScopusGoogle Scholar

27. [27]

W. Zhang, Z. Yin, A. Chun, J. Yoo, Y.S. Kim, Y. Piao

Bridging oriented copper nanowire–graphene composites for solution-processable, annealing-free, and air-stable flexible electrodes

ACS Appl. Mater. Interfaces, 8 (2016), pp. 1733-1741

CrossrefView in ScopusGoogle Scholar

28. [28]

B. Maira, K. Takeuchi, P. Chammingkwan, M. Terano, T. Taniike

Thermal conductivity of polypropylene/aluminum oxide nanocomposites prepared based on reactor granule technology

Compos. Sci. Technol., 165 (2018), pp. 259-265

View PDFView articleView in ScopusGoogle Scholar

29. [29]

X. Zhang, X. Xia, H. You, T. Wada, P. Chammingkwan, A. Thakur, T. Taniike

Design of continuous segregated polypropylene/Al2O3 nanocomposites and impact of controlled Al2O3 distribution on thermal conductivity

Compos. A, 131 (2020), Article 105825

View PDFView articleView in ScopusGoogle Scholar

30. [30]

S. Zhou, X. Zeng, X. Yan, F. Xie, B.D. Fahlman, C. Wang, W. Li

High aspect ratio copper nanowires and copper nanoparticles decorated by reduced graphene oxide for flexible transparent conductive electrodes

Appl. Surf. Sci., 604 (2022), Article 154597

View PDFView articleView in ScopusGoogle Scholar

31. [31]

M. Jin, G. He, H. Zhang, J. Zeng, Z. Xie, Y. Xia

Shape-controlled synthesis of copper nanocrystals in an aqueous solution with glucose as a reducing agent and hexadecylamine as a capping agent

Angew. Chem. Int. Ed., 50 (2011), pp. 10560-10564

CrossrefView in ScopusGoogle Scholar

32. [32]

S. Pei, H.-M. Cheng

The reduction of graphene oxide

Carbon, 50 (2012), pp. 3210-3228

View PDFView articleView in ScopusGoogle Scholar

33. [33]

D.-M. Ye, G.-Z. Li, G.-G. Wang, Z.-Q. Lin, H.-L. Zhou, M. Han, Y.-L. Liu, J.-C. Han

One-pot synthesis of copper nanowire decorated by reduced graphene oxide with excellent oxidation resistance and stability

Appl. Surf. Sci., 467–468 (2019), pp. 158-167

View PDFView articleView in ScopusGoogle Scholar

34. [34]

J. Shen, M. Shi, N. Li, B. Yan, H. Ma, Y. Hu, M. Ye

Facile synthesis and application of Ag-chemically converted graphene nanocomposite

Nano Res., 3 (2010), pp. 339-349

CrossrefView in ScopusGoogle Scholar

35. [35]

E. Kim, A. Umar, S. Ameen, R. Kumar, A.A. Ibrahim, M.A.M. Alhamami, M.S. Akhtar, S. Baskoutas

Synthesis and characterizations of ZIF-8/GO and ZIF-8/rGO composites for highly sensitive detection of Cu2+ ions

Surf. Interfaces, 41 (2023), Article 103163

View PDFView articleView in ScopusGoogle Scholar

36. [36]

M.S. Amir Faiz, C.A. Che Azurahanim, S.A. Raba'ah, M.Z. Ruzniza

Low cost and green approach in the reduction of graphene oxide (GO) using palm oil leaves extract for potential in industrial applications

Results Phys., 16 (2020), Article 102954

View PDFView articleView in ScopusGoogle Scholar

37. [37]

C. Hu, H. Zhang, N. Neate, M. Fay, X. Hou, D. Grant, F. Xu

Highly aligned Ni-decorated GO–CNT nanostructures in epoxy with enhanced thermal and electrical properties

Polymers, 14 (2022), p. 2583

CrossrefView in ScopusGoogle Scholar

38. [38]

R. Navik, X. Ding, T. Huijun, Y. Gai, Y. Zhao

Fabrication of copper nanowire and hydroxylated graphene hybrid with high conductivity and excellent stability

Appl. Mater. Today, 19 (2020), Article 100619

View PDFView articleView in ScopusGoogle Scholar

39. [39]

T. Zhang, W.-Y. Hsieh, F. Daneshvar, C. Liu, S.-P. Rwei, H.-J. Sue

Copper(i)–alkylamine mediated synthesis of copper nanowires

Nanoscale, 12 (2020), pp. 17437-17449

CrossrefView in ScopusGoogle Scholar

40. [40]

R. Navik, D. Xiao, Y. Gai, H. Tan, Y. Zhao

One-pot synthesis of copper nanowire-graphene composite with excellent stability and electrical performance for flexible electrodes

Appl. Surf. Sci., 527 (2020), Article 146694

View PDFView articleView in ScopusGoogle Scholar

41. [41]

Z. Zhu, T. Mankowski, K. Balakrishnan, A.S. Shikoh, F. Touati, M.A. Benammar, M. Mansuripur, C.M. Falco

Ultrahigh aspect ratio copper-nanowire-based hybrid transparent conductive electrodes with PEDOT:PSS and reduced graphene oxide exhibiting reduced surface roughness and improved stability

ACS Appl. Mater. Interfaces, 7 (2015), pp. 16223-16230

CrossrefView in ScopusGoogle Scholar

42. [42]

F. Qian, P.C. Lan, T. Olson, C. Zhu, E.B. Duoss, C.M. Spadaccini, T.-Y.-J. Han

Multiphase separation of copper nanowires

Chem. Commun., 52 (2016), pp. 11627-11630

View in ScopusGoogle Scholar

43. [43]

Y. Ahn, Y. Jeong, D. Lee, Y. Lee

Copper nanowire-graphene core-shell nanostructure for highly stable transparent conducting electrodes

ACS Nano, 9 (2015), pp. 3125-3133

CrossrefView in ScopusGoogle Scholar

44. [44]

L. Rivière, N. Caussé, A. Lonjon, É. Dantras, C. Lacabanne

Specific heat capacity and thermal conductivity of PEEK/Ag nanoparticles composites determined by Modulated-Temperature Differential Scanning Calorimetry

Polym. Degrad. Stab., 127 (2016), pp. 98-104

View PDFView articleView in ScopusGoogle Scholar

45. [45]

J. Kim, B.-S. Yim, J.-M. Kim, J. Kim

The effects of functionalized graphene nanosheets on the thermal and mechanical properties of epoxy composites for anisotropic conductive adhesives (ACAs)

Microelectron. Reliab., 52 (2012), pp. 595-602

View PDFView articleView in ScopusGoogle Scholar

46. [46]

S. Yang, B. Xue, Y. Li, X. Li, L. Xie, S. Qin, K. Xu, Q. Zheng

Controllable Ag-rGO heterostructure for highly thermal conductivity in layer-by-layer nanocellulose hybrid films

Chem. Eng. J., 383 (2020), Article 123072

View PDFView articleView in ScopusGoogle Scholar

47. [47]

T. Ma, Y. Zhao, K. Ruan, X. Liu, J. Zhang, Y. Guo, X. Yang, J. Kong, J. Gu

Highly thermal conductivities, excellent mechanical robustness and flexibility, and outstanding thermal stabilities of aramid nanofiber composite papers with nacre-mimetic layered structures

ACS Appl. Mater. Interfaces, 12 (2019), pp. 1677-1686

CrossrefView in ScopusGoogle Scholar

48. [48]

Y. Cui, C. Liu, S. Hu, X. Yu

The experimental exploration of carbon nanofiber and carbon nanotube additives on thermal behavior of phase change materials

Sol. Energy Mater. Sol. Cells, 95 (2011), pp. 1208-1212

View PDFView articleView in ScopusGoogle Scholar

49. [49]

J.-N. Shi, M.-D. Ger, Y.-M. Liu, Y.-C. Fan, N.-T. Wen, C.-K. Lin, N.-W. Pu

Improving the thermal conductivity and shape-stabilization of phase change materials using nanographite additives

Carbon, 51 (2013), pp. 365-372

View PDFView articleView in ScopusGoogle Scholar

50. [50]

Z. Zhu, Y. Liu, J. Ge, Z. Hu, G. Zeng, X. Peng, W. Xu, X. Peng

High dielectric polymer composites from thermal-induced in-situ formation of conjugated structures and reduced graphene oxide

Mater. Chem. Phys., 262 (2021), Article 124276

View PDFView articleView in ScopusGoogle Scholar

51. [51]

F. Xu, D. Bao, Y. Cui, Y. Gao, D. Lin, X. Wang, J. Peng, H. Geng, H. Wang

Copper nanoparticle-deposited graphite sheets for highly thermally conductive polymer composites with reduced interfacial thermal resistance

Adv. Compos. Hybrid Mater., 5 (2021), pp. 2235-2246

Google Scholar

52. [52]

X. Xu, J. Zhou, J. Chen

Thermal transport in conductive polymer–based materials

Adv. Funct. Mater., 30 (2019), Article 483001

Google Scholar